Revealing the impact of second phase morphology on discharge properties of binary Mg-Ca anodes for primary Mg-air batteries

Min Deng[a,*], Daniel Höche[a, b], Sviatlana V. Lamaka[a], Linqian Wang[a], Mikhail L. Zheludkevich[a, c]

[a] MagIC – Magnesium Innovation Centre, Helmholtz-Zentrum Geesthacht (HZG), 21502 Geesthacht,

Germany

[b] Computational Material Design, Faculty of Mechanical Engineering, Helmut-Schmidt-University

University of the Federal Armed Forces, 22043 Hamburg, Germany

[c] Institute of Materials Science, Faculty of Engineering, Kiel University, 24143 Kiel, Germany

Abstract: Mg-0.5 (wt.%)Ca alloys with different microstructures are prepared through casting followed by different cooling rates. The impact of microstructure, especially second phase morphology, on self-corrosion and discharge performance of Mg-0.5Ca alloys is investigated. The water-cooled Mg-0.5Ca alloy shows a lower self-corrosion rate than the air-cooled one and enables the Mg-air cell to possess increased utilization efficiency and enhanced energy density. Intermittent discharge tests are performed to study the battery performance after no-discharge intervals. All results indicate that the water-cooled Mg-0.5Ca cast alloy could be a promising anode material for aqueous Mg-air batteries with long-term storage and under intermittent discharge.

Key words: Mg-air battery; Phase morphology; Self-corrosion; Intermittent discharge.

* Corresponding author.
  E-mail address: Min.Deng@hzg.de (M. Deng), Telephone number: +49 (0)4152 871936, Postal address: Helmholtz-Zentrum Geesthacht, Max-Planck-Str. 1, 21502 Geesthacht, Germany.

1. Introduction

Aqueous primary Mg-air batteries have attracted attention for some time due to their high theoretical energy density (6.8 kWh kg^{-1} based on anode), discharge voltage (3.1 V), volumetric capacity of metallic Mg (3832 mA h cm^{-3}, vs. 2061 mA h cm^{-3} for Li) and relatively low cost [1-3]. Despite these advantageous characteristics, the spread of this technology is rather limited because of a number of critical obstacles related to the self-corrosion and discharge kinetics of metallic Mg-based anodes. A number of research works have been dedicated to overcoming the limitations of Mg-air batteries for practical applications, such as poor self-corrosion resistance and surface blockage of the anode. Performance boost for the primary Mg-air system can be achieved by developing novel Mg anodes [4-7] as well as tailoring electrolyte compositions [8-13]. During the past decades, several types of Mg alloys have been proposed for use in Mg-air systems, i.e., Mg-Al-Zn [14, 15], Mg-Al-Pb [16], Mg-Al-Sn [17-19] and Mg-Li [20-22]. Nevertheless, the practical voltage and specific capacity of such systems are still much lower than the theoretical values. In addition, the Pb commonly used in Mg-Al-Pb alloys is harmful to the environment despite its positive impact on the discharge voltage of Mg-air batteries. Furthermore, in terms of Mg-Li anodes, quaternary or even quintenary alloys doped with several alloying elements, like Zn, Y, Ce or Al, are necessary to ensure both a high voltage and low self-corrosion rate. The large amount of alloying elements that have a higher density than Mg would decrease the gravimetric capacity of the Mg anodes and substantially reduce the technical tolerances, leading to a large increase in associated costs. In this context, novel binary Mg-Ca anodes with a minor amount of Ca (less than 0.5 wt.%) were proposed in our previous work [23], in which battery performance as a function of different anodes was compared. The results demonstrate the application potential of Mg-Ca anodes due to their superior discharge performance compared to that of high-purity Mg and some commercial magnesium alloys.

It is well known that the microstructure, including the grain size, second phase morphology and distribution, has a great effect on the corrosion resistance and electrochemical performance of Mg alloys. Therefore, microstructure tuning through various processing methods, e.g., heat treatment and plastic deformation, has become the most popular approach to improve the discharge properties of Mg anodes [15, 24-27]. As demonstrated by Huang et al. [14], an as-rolled AZ31 anode shows a higher discharge activity and voltage than the as-cast material when acting as the anode for a Mg-air battery. Regarding Mg-Ca alloys, the impact of microstructure on corrosion resistance has been widely investigated, but most studies were performed on Mg-Ca alloys with high Ca contents ($\geq$ 1 wt.%) and in biomedical solutions [28-31]. Jeong et al. [31] studied the effect of microstructural refinement on the corrosion resistance of Mg-Ca alloys by indirect extrusion. No improvement in the corrosion resistance for a Mg-0.4 wt.% Ca alloy in Hank's solution was found in this research, and they attributed this to the competition between grain refinement and increased dislocation and twin densities.

Nevertheless, the influence of second phase morphology and distribution in Mg-Ca alloys with a low Ca content is still unclear. To the best of our knowledge, no research has revealed the effect of the microstructure on the discharge properties of Mg-Ca anodes for primary Mg-air systems. Therefore, the aim of this work is to investigate the effect of the microstructure, especially the second phase morphology and distribution, on the self-corrosion rate of binary Mg-Ca alloys as well as their capability as an anode material. In addition, the application prospect of Mg-Ca alloys is also studied when serving as anodes for aqueous Mg-air batteries with long storage times under intermittent discharge. The Mg-0.5 wt.%Ca alloy was chosen as the research object in this work to ensure a relatively high content of the second phase because the effect of the second phase morphology is the emphasis here. This composition is still in the range of the optimized alloy composition of binary Mg-Ca anode, i.e., Mg-(0.1~ 0.5) wt.%Ca,

as concluded in our previous work [23], which indicated only a slight difference between the discharge properties of Mg-0.1Ca and Mg-0.5Ca alloy anodes.

2. Experimental procedures

2.1 Materials preparation

Mg-0.5Ca alloys with nominal composition of Mg-0.5 wt.% Ca were prepared through conventional casting with a pure Mg ingot (99.96 wt. %) and pure Ca chips (99.0 wt. %). The raw materials were placed in a steel crucible protected by Ar and SF_6 mixed gas and then heated to 760 °C. Before casting, the melting metal was stirred for 5 min to ensure composition homogeneity. Afterwards, to obtain Mg-0.5Ca alloys with identical compositions but different microstructures, the melt was cast into two moulds with different cooling methods, i.e., in air and in water. The mould for air cooling was cylindrical with a diameter of 18 mm and a thickness of 10 mm, while the mould for water cooling was cylindrical with a diameter of 60 mm and a thickness of 6 mm. The bottom and top portions for each prepared ingot with a length of 20 mm were discarded due to the possible accumulation of impurities and oxide. Specimens for all experiments were extracted from the rest of the ingots after removing the surface oxide. The chemical composition of the prepared materials is presented in Table 1. Ca was detected with atomic absorption spectroscopy, while other elements were measured by optical emission spectrometry. The content of impurities, which have a substantial influence on Mg corrosion [13, 32, 33], were low and below their tolerance limitations. The two alloys that were air cooled and water cooled are referred to as AC and WC alloys, respectively.

Table 1 Chemical composition of Mg-0.5Ca alloy (wt.%).

Material	Ca	Fe	Ni	Cu	Si	Mn	Al	Mg
Mg-0.5Ca	0.50	0.0015	0.0009	0.0016	0.011	0.033	<0.01	Bal.

2.2 Microstructure observation

The corresponding microstructures of the prepared alloys were characterized via optical microscopy (OM) and scanning electron microscopy (SEM). To obtain samples with a high quality, all the specimens embedded in epoxy were ground with 4000 grit silicon carbide paper followed by a polishing process with the assistance of a water-free SiO_2 oxide polishing suspension (OPS). All the specimens after polishing were immersed in ethanol and cleaned by ultrasonication. Afterwards, an acetic-picric acid solution was used for sample etching before optical microscopy analysis. The grain sizes were determined through the average grain intercept (AGI) method. In the case of both alloys, five pictures were collected with OM and then utilized to calculate the average grain size. Additionally, element analysis for second phase particles was carried out with energy dispersive X-ray spectrometry (EDX).

2.3 Immersion tests

The corrosion rates of the Mg-0.5Ca alloys were evaluated at a free corrosion potential and room temperature using the hydrogen collection method after immersion in a 3.5 wt.% NaCl solution. The experimental configuration used here is similar to that commonly used for studying Mg corrosion [17, 34]. An inverted burette with a funnel covering the corroding sample was used to collect the evolved hydrogen during the immersion period. Each sample with a surface area of nearly 8 cm^2 was suspended and completely exposed in the solution through a fishing line and a plastic screw with a diameter of 2.5 mm. Crevice corrosion was avoided with this specimen configuration that was proposed by Shi et al. [35]. Before the hydrogen evolution test, each sample was ground with SiC sandpapers up to 1200 grit. The weight loss of each specimen after the immersion test was measured after removing the corrosion products in a diluted chromic acid solution (200 g L^{-1}). In addition, the surface morphology of each alloy after immersion for a short time was also recorded with SEM to

study the origination and propagation of the corrosion. Before exposure to the solution, each sample was polished to remove most scratches. Samples after the hydrogen evolution measurement were also observed with SEM after removing the corrosion products.

2.4 Electrochemical impedance spectroscopy (EIS)

EIS measurements after discharge were performed with a potentiostat (Gamry, USA) to compare the discharge activity of the Mg-0.5Ca alloys. A typical three-electrode system was applied with the specimen serving as the working electrode. The reference and counter electrodes were saturated Ag/AgCl and Pt plates, respectively. After the specimens were ground with 1200 grit sandpaper, they were exposed to the solution with a working surface area of 1 cm^2. The samples were scanned from a high frequency (100 kHz) to a low frequency (0.01 Hz), and the sinusoidal excitation voltage was 10 mV rms. Three separate samples of each Mg-0.5Ca alloy were used for EIS measurement to ensure reproducibility.

2.5 Mg-air battery tests

A full cell constructed in the laboratory was used to compare the discharge properties of the magnesium-air system using the Mg-0.5Ca alloys as the anode. A conventional air cathode comprising a gas diffusion layer, a C/MnO$_2$ catalyst layer and a nickel mesh current collector layer was utilized. A 3.5 wt.% NaCl solution was adopted as the electrolyte. The working surface area of the anode for all discharge tests was approximately 2.5 cm^2. Discharge curves at different current densities, i.e., 2 mA cm^{-2} and 10 mA cm^{-2}, were recorded using a Gamry interface 1000 potentiostat. After discharge, the corrosion products on the anode surface were removed in a 200 g L^{-1} chromic acid solution. Afterwards, the specific energy density (based on the anode only) as well as the anode utilization efficiency were calculated. The following equations were used [36, 37]:

$$\text{Utilization efficiency (\%)} = \frac{W_{theo}}{\Delta W} \times 100\% \tag{1}$$

$$\text{Specific energy density (Wh kg}^{-1}\text{)} = \frac{\int_0^t U \times I \times \Delta t}{\Delta W} \qquad (2)$$

where U (V) represents the instantaneous cell voltage corresponding to discharge time t (h), I (A) is the applied current, ΔW (kg) represents the specific anode mass loss during each measurement, and W_{theo} (kg) is the theoretically consumed anode mass attributed to the faradaic process. The value of ΔW was obtained via the measured weight of the specimens before the discharge test and after removal of the discharge products. The theoretical weight loss W_{theo} was obtained via the equation [38, 39]:

$$W_{theo} \text{ (kg)} = \frac{I \times t}{F \times \sum(\frac{x_i \times n_i}{m_i})} \times \frac{1}{1000} \qquad (3)$$

where F is the Faraday constant (26.8 Ah mol^{-1}); and m_i (g mol^{-1}), n_i and x_i are the atomic mass, number of exchanged electrons and mass fraction relevant to Mg and each alloying element, respectively.

Surface morphologies and corresponding corrosion sections of samples after discharge were recorded with SEM as well. In addition, an intermittent discharge test was also carried out for Mg-air batteries with both Mg-0.5Ca anodes at 2 mA cm^{-2}. In each cycle, the discharge process lasted for 10 hours followed by a no-discharge period of 5 hours. Five cycles were tested to evaluate the stability of Mg-Ca relevant batteries during long-term usage.

3. Results

3.1 Microstructure

Two different microstructures were obtained by the different cooling methods, as indicated by Fig. 1. The optical images (see Fig. 1(a, d)) show that water cooling slightly decreases (by ca. 16%) the grain size of this alloy compared to air cooling. The calculated grain size is 577 $\pm$ 180 µm for the AC alloy and 438 $\pm$ 53 µm for the WC alloy (average of three samples from
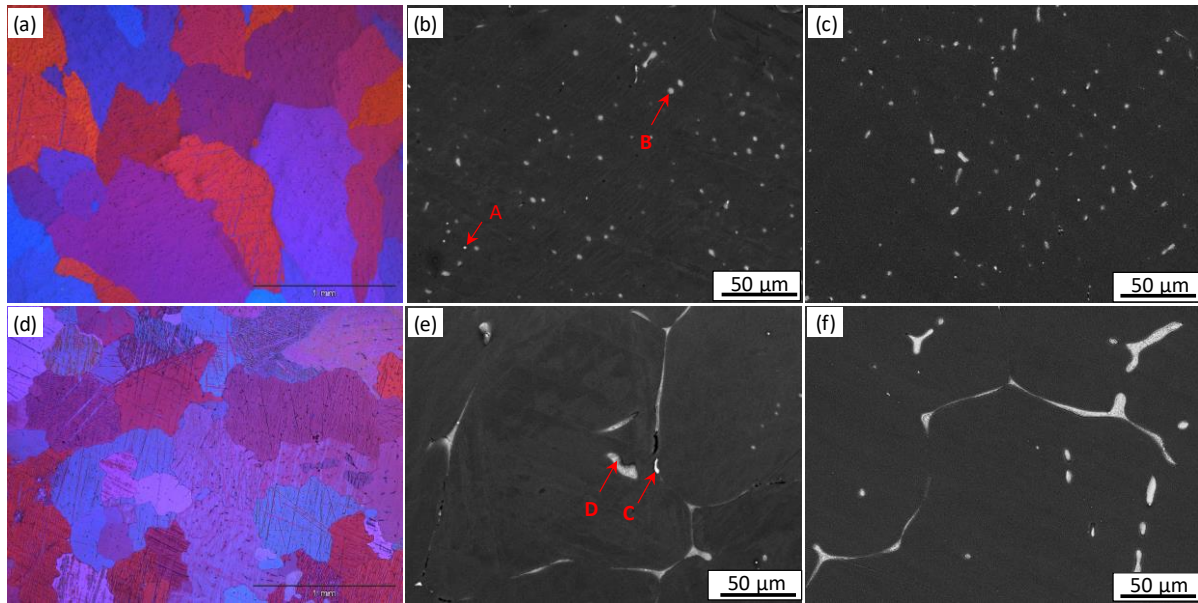
Fig. 1. Optical and SEM images of Mg-0.5Ca alloys: (a, b, c) AC; (d, e, f) WC. (b, e) SEM images of ingot horizontal plane; (c, f) SEM images of ingot vertical plane. Table g is the EDX results for particles marked A, B, C and D.

different locations). Furthermore, the morphology and distribution of the second phase, which is generally an α-Mg/Mg$_2$Ca eutectic aggregate [23, 40, 41], also varied with different cooling methods, as demonstrated by the scanning electron microscopy images (see Fig. 1(b, c, e, f)). It is noteworthy that for both materials, the second phase morphology corresponding to the ingot horizontal plane and vertical plane are identical. For the AC material, a large number of fine second phase particles is distributed uniformly in the matrix. In contrast, for the WC material, except for a few second phase particles in the grain interior, most of the second phase is relatively continuous and is distributed along grain boundaries as dendrites. Nevertheless, the grain boundaries are not fully populated by the second phase because of its insufficient amount due to the relatively low Ca content. In other words, grains in the Mg-0.5Ca WC alloy

are not completely surrounded by continuous second phases. Specimens from the centre and edge of the WC alloy ingot also exhibit the same second phase morphology, indicating good ingot homogeneity. The only difference is the slightly larger grain size of the specimen from the edge (485 ± 122 µm) compared to that from the ingot centre (381 ± 65 µm). In addition, except for the α-Mg/Mg₂Ca eutectic phase, some small impurity-rich particles with compositions of Mg-Ca-Si or Mg-Ca-Si-Fe are also found in both materials. This is consistent with the description on the microstructure of the Mg-0.8 wt.% Ca alloy by Mohedano et al. [41] and Mg-0.54 wt.% Ca alloy by Zeng et al. [42]. As shown in Fig. 1(g), the EDX results of points A and C, as marked in the SEM images, also prove the existence of Mg-Ca-Si particles. Mg-Ca-Si-Fe particles are not noted here because of their low quantity due to the low Fe content in both alloys. Particles B and D with larger sizes are regular α-Mg/Mg₂Ca eutectic phases, as shown by the EDX results.

3.2 Hydrogen evolution

Fig. 2 presents the hydrogen evolution results of the Mg-0.5Ca alloys obtained with different cooling methods. Two samples of both materials were tested in parallel under the same experimental conditions to ensure the reproducibility of the results. At the initial stage of immersion (nearly three hours), the WC alloy suffers a higher hydrogen evolution rate, indicating a faster corrosion rate than the AC alloy. Thereafter, the hydrogen evolution rate of the WC alloy slows down and is surpassed by that of the AC alloy. During the later immersion period, both materials show relatively stable hydrogen evolution rates. Concerning the whole 7-day immersion test, the WC alloy evolved less hydrogen than the AC alloy, showing that the former had a lower average corrosion rate than the latter in the 3.5 wt. % NaCl solution. With the hydrogen evolution rate, the self-corrosion rate of these two materials can be deduced according to the equation P_H (mm y^{-1}) = 2.088 V_H (ml cm^{-2} d^{-1}) [43]. The average corrosion rate obtained from hydrogen evolution data is 0.15 mm y^{-1} for the WC Mg-0.5Ca alloy and

0.26 mm y^{-1} for the AC material. It should be noted that the corrosion rate could be underestimated with the hydrogen evolution method, especially for Mg alloys with a high corrosion resistance [44, 45]. In this case, corrosion rates of these alloys were also determined according to results of weight loss measurement via the conversion P_W (mm y^{-1}) = 2.1 ΔW(mg cm^{-2} d^{-1}) [43]. The measured corrosion rate is 0.20 mm y^{-1} for the WC alloy and 0.31 mm y^{-1}

for the AC alloy, both are lower than the corrosion rate of most Mg alloys in similar solutions, as summarized by Cao and co-workers [46]. A low corrosion rate of the anodes during the no-discharge period is crucial for the aqueous primary Mg-air system to increase its service life. Therefore, the remarkably low overall corrosion rate enables Mg-0.5Ca alloys to
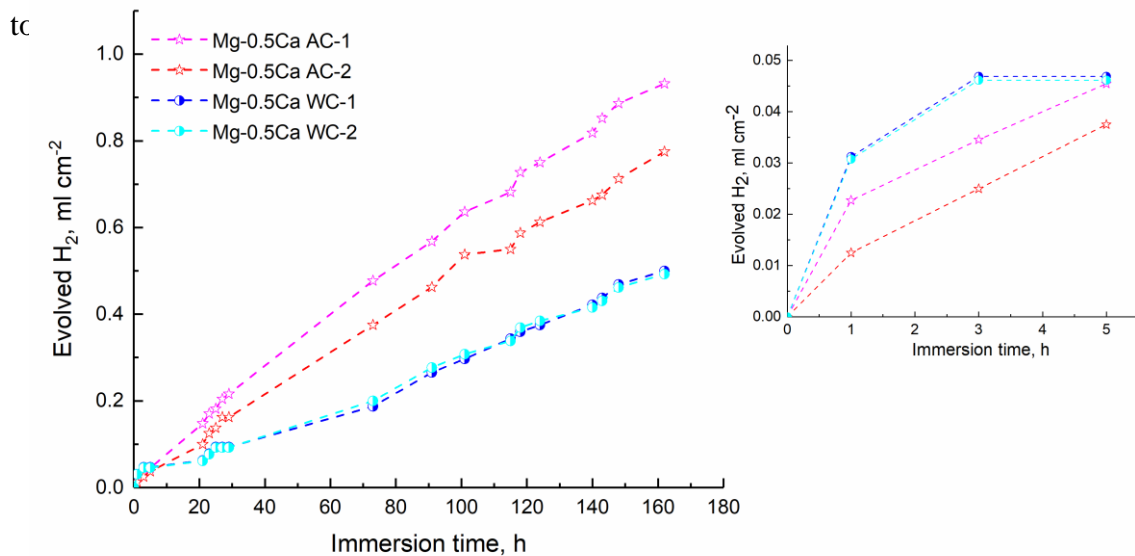

Fig. 2. Hydrogen evolution of Mg-0.5Ca alloys in 3.5 wt.% NaCl solution (unbuffered, pH 5.6).

3.3 Mg-air battery properties

The cell voltage and specific energy density of the battery based on different Mg-0.5Ca anodes were tested and are presented in Fig. 3. A drastic difference is not found between the cell voltages of the electrochemical system with these two anode materials, except that the

battery with AC anode shows gradually increasing voltage, while the voltage for that with WC material is relatively stable. Nevertheless, apparent differences can be found regarding the utilization efficiency as well as the specific energy density based on the anode materials during the discharge process (see Fig. 3b). The WC anode shows higher utilization efficiency than the AC anode at both current densities. Compared to that of the ordinary air cooling, the water cooling increases the utilization efficiency of the Mg-0.5Ca anode from 37.1% to 44.5% at a low current density of 2 mA cm^{-2}. At a higher current density, i.e., 10 mA cm^{-2}, the increase in the utilization efficiency is less pronounced, approximately 5.7%. In the case of specific energy density, the variation is similar. The battery system based on the WC anode supplies a higher energy density than that based on the AC material, especially at lower current density.
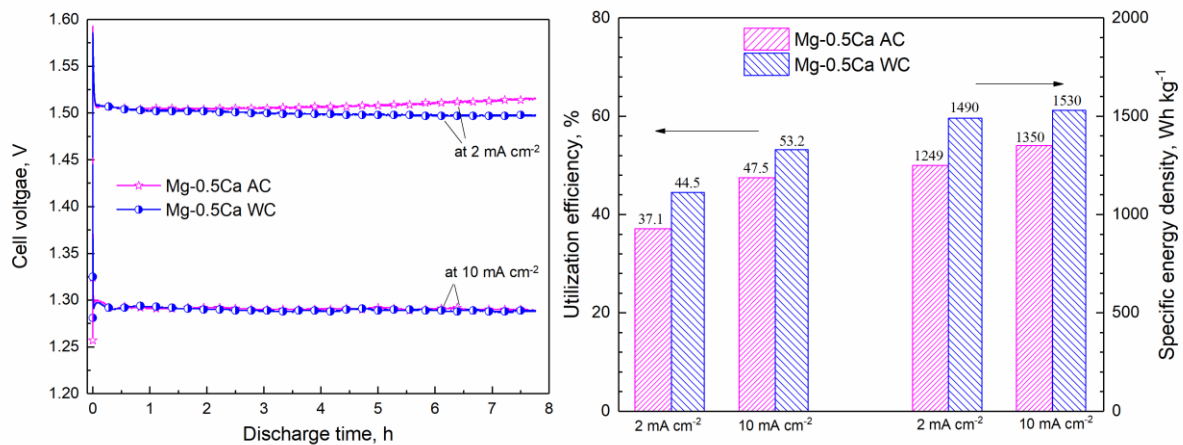

Fig. 3. Mg-air battery performance corresponding to Mg-0.5Ca anodes: (a) cell voltage; (b) utilization efficiency and energy density. 3.5 wt.% NaCl solution is adopted as the electrolyte, while C/MnO$_2$ acts as catalyst in the air cathode.

The intermittent discharge behaviour of the batteries operating with the AC and WC alloy anodes at 2 mA cm^{-2} are presented in Fig. 4. Similar to the results presented in Fig. 3a, the cell voltage based on the AC anode increases gradually during every discharge period. However, its average voltage is found to decrease with increasing number of discharge cycles. For instance, the average voltage in the first discharge cycle is 1.506 V, while in the fifth discharge cycle it is 1.485 V. Such change is not as obvious for the intermittent discharge of the battery

based on the WC anode. The average voltage is 1.499 V for the first discharge cycle, while it is 1.490 V for the fifth cycle. In other words, this battery system can maintain a stable voltage even after several closed/opened circuit cycles, which is important for the practical application of battery systems concerning sporadic switch-on and switch-off operation. In addition, the OCV of the battery with the AC anode is higher than that based on the WC anode in all intervals between the discharge processes.
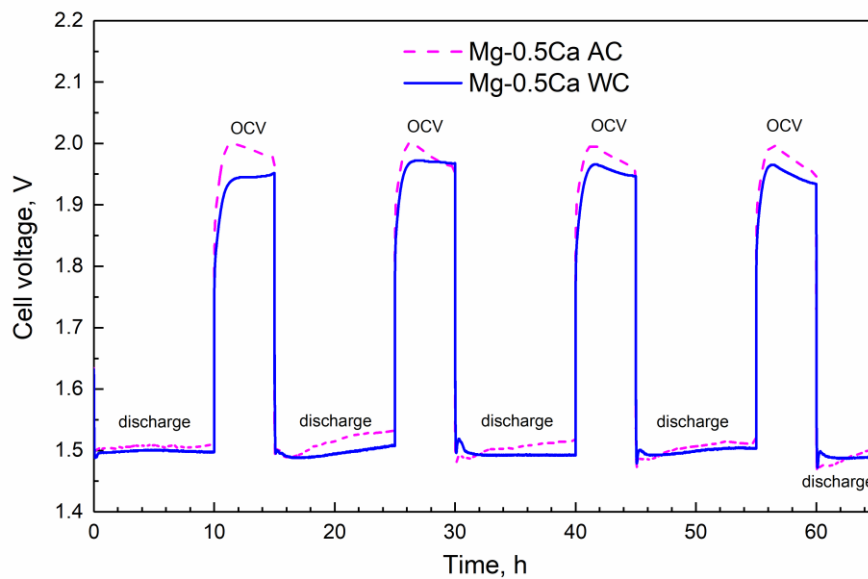

Fig. 4. Intermittent discharge curves of lab-made Mg-air cells adopting Mg-0.5Ca anodes with applied 2 mA cm^{-2} current density. 3.5 wt.% NaCl solution is adopted as the electrolyte, while C/MnO$_2$ acts as catalyst in the air cathode.

4. Discussion

4.1 Effect of microstructure on corrosion behaviour

It is well known that a faster solidification rate leads to finer grains due to the increased nucleation rate and decreased time for grain growth [47-49]. Therefore, the Mg-0.5Ca sample prepared with water cooling shows a smaller grain size than that prepared through air cooling. In addition, the solidification rate can also significantly affect the second phase morphology. For the alloy prepared with air cooling, the α-Mg solid solution is saturated with Ca atoms at a

high temperature. During the slow solidification process, the Ca distributed uniformly in the Mg matrix and precipitated as Mg_2Ca particles due to the low solid solubility of calcium in a magnesium matrix at low temperature. By contrast, when prepared with water cooling, the faster cooling rate caused a greater segregation of the solute atoms [50] (Ca atoms in this study) and that led to the precipitation of Ca as a coarse α-Mg/Mg_2Ca eutectic structure.

The surface morphology after immersion for different times was recorded and is presented in Fig. 5 to demonstrate the dissolution process of the Mg-0.5Ca alloys. To observe the dissolution process at the very initial stage, diluted NaCl solution with a concentration of 0.5 wt.% was utilized. The surface morphologies after exposure in 0.5 wt.% NaCl solution for 5 min and 30 min are demonstrated in Fig. 5(a-d). It can be seen that the corrosion of both materials begins at some preferential points, in which impurity particles exist, as proven by the inserted EDX maps. This is reasonable because these impurity-rich particles have a large potential difference with the Mg matrix [41] and become the driving force for galvanic corrosion. Thereafter, the Mg_2Ca phases undergo corrosion due to their higher negative potential than the Mg matrix [30, 51, 52], which renders the Mg_2Ca to be the anode that preferentially undergoes corrosion in the micro-galvanic cell coupled with Mg matrix. After exposure to a 3.5 wt.% NaCl solution for 24 hours, both Mg-0.5Ca alloys show surfaces covered with thin but compact oxide films with few micro-cracks, in addition to some coarse corrosion products in the sites that experienced galvanic corrosion (see Fig. 5e and f)). As reported, Ca-containing Mg alloys typically exhibit a protective calcium carbonate film on the surface after immersion [53]. Furthermore, the surface morphologies of both alloys after immersion for 7 days and removal of the corrosion products are also shown in Fig. 5g and h. Scratches left by the mechanical grinding are still apparent on the surface of both alloys even after 7 days of immersion, which is further evidence of the low self-corrosion rates of these two Mg-0.5Ca alloys prepared via different cooling routes. However, the AC alloy experienced
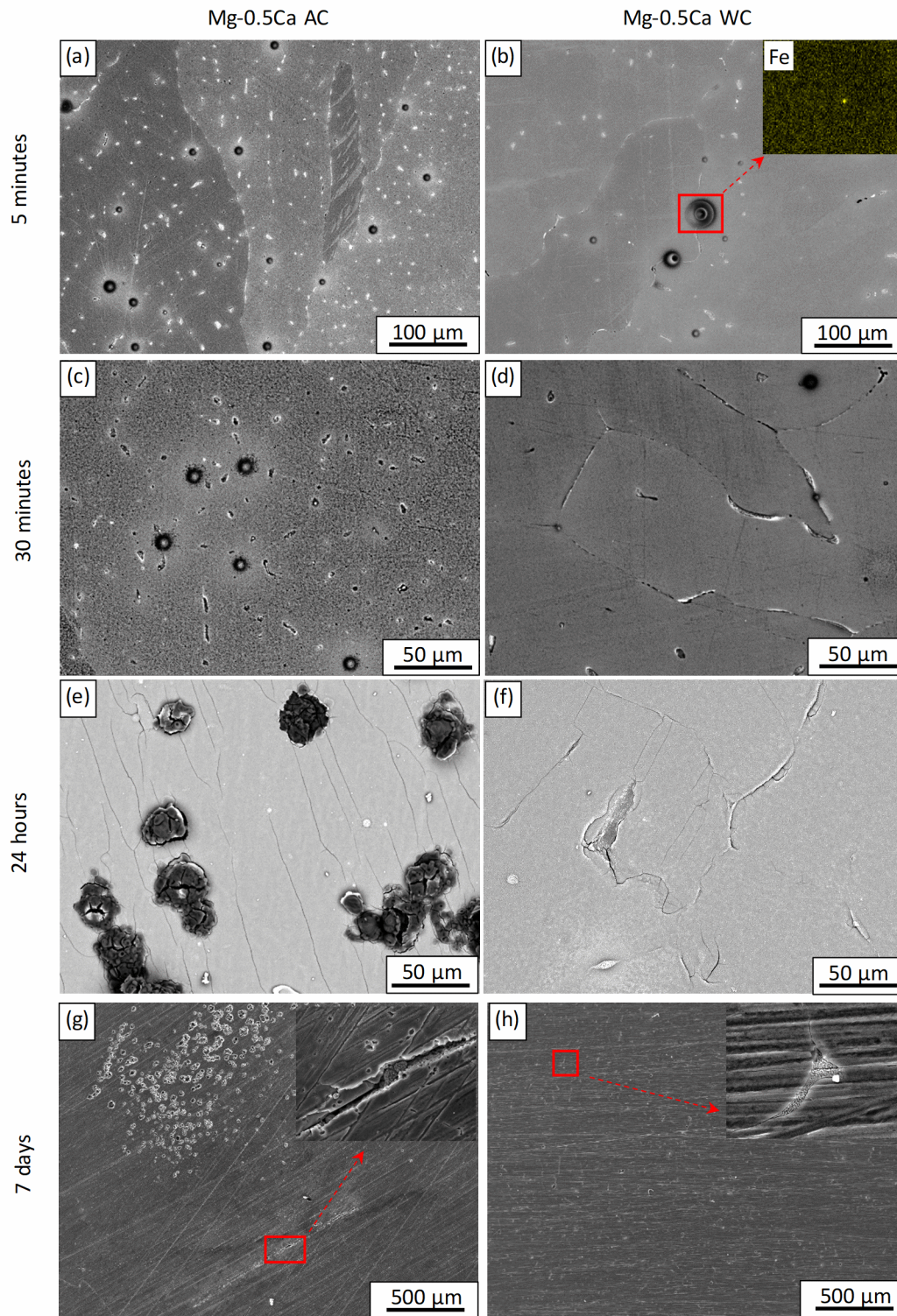
Fig. 5. Surface morphology of Mg-0.5Ca alloys after immersion for different time in: (a-d) 0.5 wt.% NaCl solution; (e-h) 3.5 wt.% NaCl solution. The surfaces after 7-days immersion are recorded after removing corrosion products. The inserted image in (b) is the EDX mapping for Fe, while in (g, h) it is corresponding enlargement of marked area.

localized corrosion to some extent, leaving a number of cavities and one corrosion strip on the surface, as shown in Fig. 5g. In contrast, the corrosion is more general and uniform on the WC alloy. The Mg_2Ca phases are still visible in the dendrites along the grain boundaries (see the inserted enlargement in Fig. 5h).

In conclusion, both the hydrogen evolution and surface morphologies indicate that the corrosion rates of Mg-0.5Ca alloys decrease after immersion for several hours due to the protective oxide/hydroxide film that formed on the alloy surface. The Mg-0.5Ca alloy processed with water cooling has a slower average corrosion rate than the AC alloy after a long immersion time, even though it reverses at the initial stage of several hours. Grain size is not the crucial factor for the different corrosion rates of the Mg-0.5Ca alloys because the grain refinement caused by water cooling is slight. Instead, the morphology and distribution of the second phases act as key factors for the various corrosion behaviours of the Mg-0.5Ca binary alloys. Concerning the initial exposure period in solution, the WC alloy shows a higher dissolution rate due to the presence of the continuous active Mg_2Ca phases along grain boundaries. Compared to the fine Mg_2Ca particles distributed uniformly in the AC alloy, the large second phases in the WC alloy expose a larger surface area of the anodic phases to the solution, leading to a faster overall hydrogen evolution rate. With increasing immersion time, the formation of a protective film suppresses the corrosion rates of both the WC and AC Mg-0.5Ca alloys. However, the corrosion rate of the AC material becomes higher than that of the WC material. This can be attributed to the propagation of pitting or localized corrosion caused by more impurity-rich particles and smaller Mg_2Ca particles in the AC alloy. As stated by Seong and Kim [54], there is a greater probability of isolated corrosion pits left by the dissolution of small Mg_2Ca particles that connect to form large and deep pits.

4.2 Effect of microstructure on utilization efficiency and energy density

The experimental results shown in the previous section indicate that both the utilization efficiency and energy density of the WC Mg-0.5Ca alloy are higher than those of the AC alloy at different current densities. Generally, the energy density of the Mg-air battery relates to the utilization efficiency of the electrodes as well as the cell voltage. In the case of this research, the battery voltage corresponding to the AC and WC alloy anodes has no significant difference, so the energy density depends only on the utilization efficiency of the anodes. According to equation (1), the utilization efficiency is inversely proportional to the actual weight loss of the anode during discharge. Actually, the weight loss during discharge consists of three parts, namely, the weight loss caused by impressed discharge current, the weight loss by self-corrosion of the Mg anodes and the weight loss due to the detachment of undissolved grains (known as the "chunk effect") [16, 23, 55, 56]. The chunk effect is also a kind of self-corrosion process occurring via different mechanisms. Therefore, the lower corrosion rate of the WC alloy measured in 3.5 wt.% NaCl solution at OCP could partly contribute to its higher utilization efficiency than that of the AC anode. To explore the contribution of the chunk effect, the surface morphologies of these two materials after discharge are shown in Fig. 6. It is remarkable that the surface of the AC anode after discharge and removal of the discharge products is rugged (see Fig. 6a), while the surface of the WC anode is more even in spite of some relatively small cavities (see Fig. 6b). From the cross-section presented in Fig. 6c, some undissolved grains can be found in the discharge product layer of the AC anode. These undissolved grains can detach from the anode surface into the solution along with the falling down of discharge products. In this way, they do not participate in the discharge process of Mg anodes and therefore decrease the utilization efficiency. In contrast, few undissolved grains can be found for the WC material (see Fig. 6d), indicating a slight impact of the chunk effect. In addition, for both anodes, there are some discharge cracks penetrating down into the anode substrate, as shown by the enlarged BSE images of the marked areas. These cracks or discharge

channels are most likely along the grain boundaries, as demonstrated by the presented corresponding optical images. The discharge channels in the AC anode appear broad and shallow, while in the WC anode, the channels appear narrow and deep into the matrix.
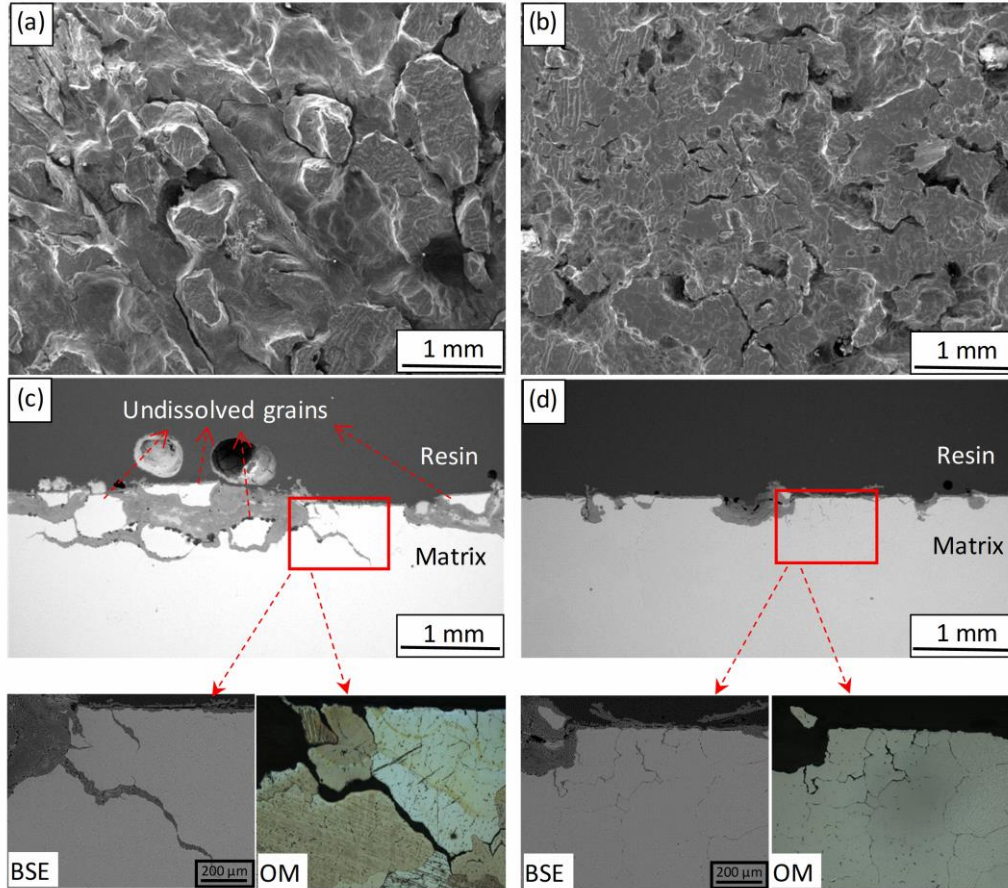

Fig. 6. Surface morphologies and cross sections of Mg-0.5Ca alloys (a, c) AC, (b, d) WC after discharge in 3.5 wt.% NaCl solution at 2 mA cm^{-2} for 16 hours: (a, b) surface after removing discharge products; (c, d) cross-section with discharge products. Corresponding SEM and OM images of marked areas are also presented.

To investigate the formation process of these two different discharge morphologies, the surfaces and corresponding cross-sections after discharge at 2 mA cm^{-2} for different times, i.e., 30 min, 2 h and 6 h, are presented in Fig. 7. For both Mg-0.5Ca alloys, discharge cracks appear after discharge for 30 min (see Fig. 7(a, b)). After that, these cracks show extraordinarily different propagation behaviours. In terms of the AC alloy, these cracks become large and deep with increasing discharge time (Fig. 7c). Gradually, these growing cracks connect with each

other (Fig. 7e), and some matrix grains start to detach from the anode surface because of the connection of the large cracks (see cross-sections in Fig. 6 and Fig. 7). In the case of the WC anode, no large discharge cracks are found in Fig. 7(d, f). Instead, most of these discharge cracks prefer to penetrate deeply into the anode matrix along the grain boundaries (see Fig. 6d). Therefore, the surface after discharge is more even. The utilization efficiencies of these two anodes after discharge for different times are also calculated and presented in Fig. 8. A discussion of the difference between the calculated utilization efficiency after a 0.5-hour discharge is not meaningful since an experimental error may exist due to the small amount of weight loss after a short discharge. The changing utilization efficiency after long-term discharge deserves more discussion to evaluate the discharge behaviour of these two anode materials. The WC anode shows increased utilization efficiency from a 2-hour discharge to a 6-hour discharge, which could be attributed to the increased surface area after the discharge process. In principle, an increased surface area leads to a decreased applied current density, i.e., a weakened polarization. It is well known that Mg and Mg alloys under polarization suffer from fast self-corrosion because of the negative difference effect (NDE) [33, 57, 58]. The self-corrosion rate is related to the extent of polarization or anodic current density. A positive correlation relationship is expected. Therefore, to some extent, self-corrosion of the WC anode might decrease with prolonged discharge time due to the reduced current density caused by the increased surface area. After that, the WC anode can maintain a relatively stable utilization efficiency with increasing discharge time, owing to the balance between the slightly increased surface area and the weak chunk effect. By contrast, the utilization efficiency of the AC anode is similar to that of the WC anode after discharge for 2 hours but becomes much lower after a long discharge period. This is most likely due to the emergence of a severe chunk effect after long-term discharge, as shown in Fig. 6 and Fig. 7. The positive effect of an increased surface area on the utilization efficiency is counteracted.
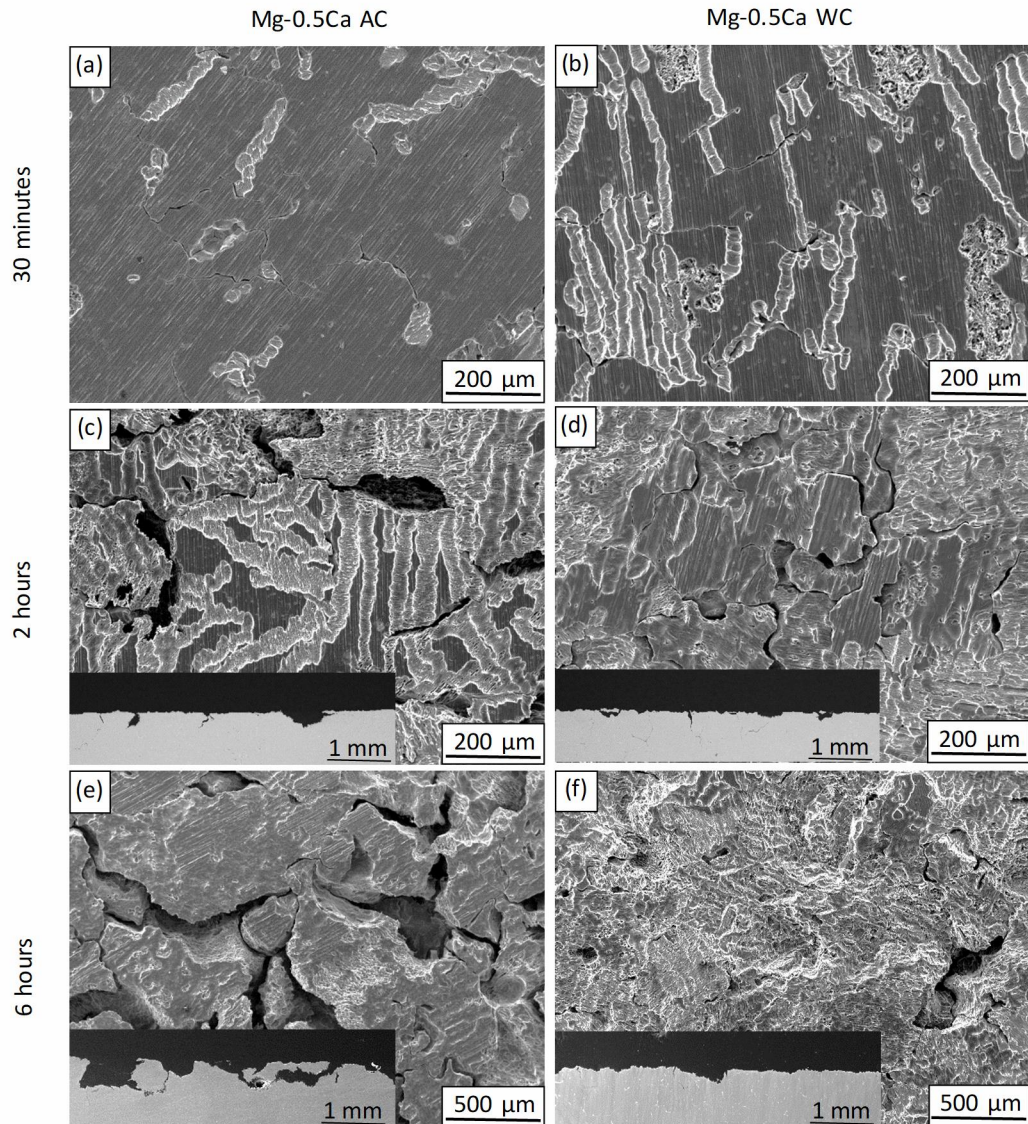
Fig. 7. Surface morphologies of Mg-0.5Ca alloys after discharge in 3.5 wt.% NaCl solution at 2 mA cm^{-2} for different time and removing discharge products. The inserted images are correspongding cross sections, in which the dark area is resin and the gray area is Mg substrate.

Based on the aforementioned discussion, a schematic illustration is proposed to describe the propagation of discharge cracks originating in the Mg-0.5Ca anodes, as shown in Fig. 9. Regarding the AC anode, crack propagation can be described as follows. (1) After application of the loading current, dissolution preferentially occurs along the grain boundaries because of the existence of active Mg$_2$Ca particles as well as the possibility of grain boundaries functioning as local anodes with respect to the Mg matrix [54, 59, 60]. Therefore, some

discharge cracks originate underneath the anode surface. (2) Thereafter, because of the discontinuity of the Mg_2Ca particles, the extension of discharge cracks slows, and the dissolution develops towards the interior area of the Mg matrix, leading to shallow but spacious cracks. (3) With increasing discharge time, these large cracks connect with each other, resulting in separated grains in the centre of the cracks. These undissolved grains then detach from the anode surface and do not participate in the discharge process. In the case of the WC anode, discharge cracks originate for the same reason. However, because the active Mg_2Ca phases are distributed relatively continuously along the grain boundaries, the cracks continue growing along the grain boundaries due to the preferential dissolution of the anodic second phases. In this case, the discharge cracks in the WC anode prefer to penetrate deep into the bulk anode instead of becoming spacious towards the interior area of the grains. It is worth noting that, in fact, grains in the WC Mg-0.5Ca anode are not completely surrounded by the α-Mg/Mg_2Ca eutectic (see Fig. 1(e, f)) because of the low content of Ca (volume fraction of second phase is not high enough). Therefore, most cracks that surround grains are not completely connected with each other. In other words, during discharge, most grains are not fully surrounded by cracks in every dimension because of the partially continuous second phases. These single grains can still keep contact with the bulk anode in some positions, contributing to the immobility of grains in the top layer. Consequently, the dissolution of the WC anode is uniform with little detachment of the grains. It was reported previously that in Mg-Ca anodes with a high Ca content, grains would detach from the anode matrix because of the preferential dissolution of Mg_2Ca phases fully surrounding these grains [23]. Note that these two propagation processes merely predominate in Mg-0.5C anodes prepared via air cooling and water cooling, respectively, which means they also happen in the other anode material to some extent.
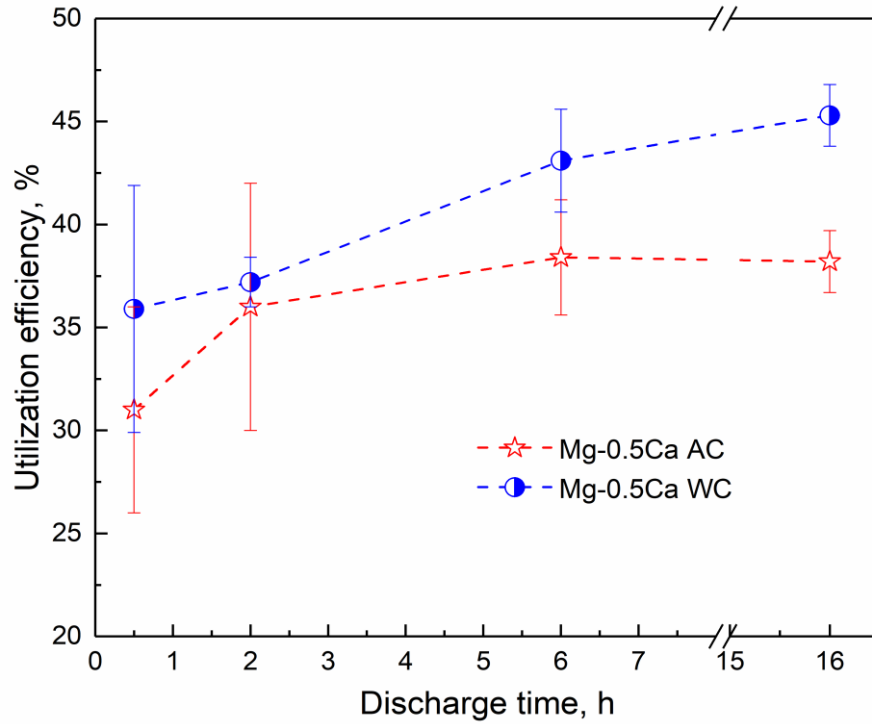
Fig. 8. Utilization efficiency of Mg-0.5Ca anodes relevant to differet discharge time in 3.5 wt.% NaCl solution at current density of 2 mA cm^{-2}.
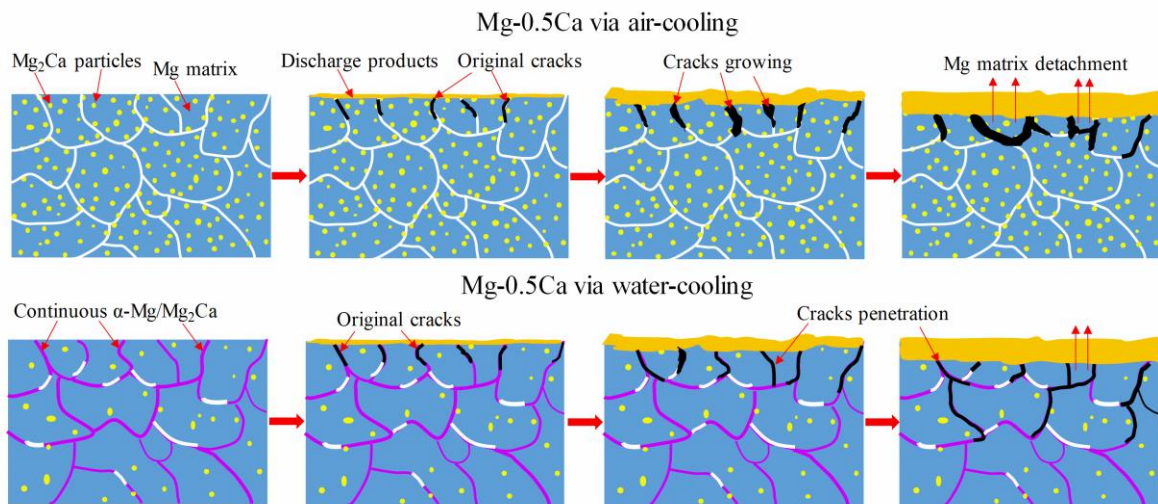

Fig. 9. Schematic illustration of the propagation process of discharge cracks in Mg-0.5Ca anodes.

4.3 Effect of microstructure on discharge voltage

The intermittent discharge curves show that the Mg-air cell utilizing the AC alloy as the anode has an enhanced OCV than that based on the WC anode, but their discharge voltages

have no apparent difference. This result could be attributed to the different discharge activities of these two anodes that can be determined by EIS spectra measured after discharge. Fig. 10 shows EIS Nyquist plots of both anodes after discharge at 2 mA cm^{-2} for 1 hour. The WC anode shows a lower resistance than the AC anode, indicating a higher dissolution activity (or lower overpotential) during discharge. Therefore, the battery system with the WC anode shows a similar cell voltage to that based on the AC anode. It is well known that a current or polarization applied to Mg anodes could cause a rupture of the oxide film on the metal surface [61, 62]. Hence, with a low protection of the oxide film, the WC Mg-0.5Ca anode could exhibit higher dissolution activity owing to the relatively continuous α-Mg/Mg$_2$Ca phases. In addition, the unstable discharge voltage of the cell incorporating the AC alloy anode may be ascribed to the increasing surface area caused by the large discharge cracks.
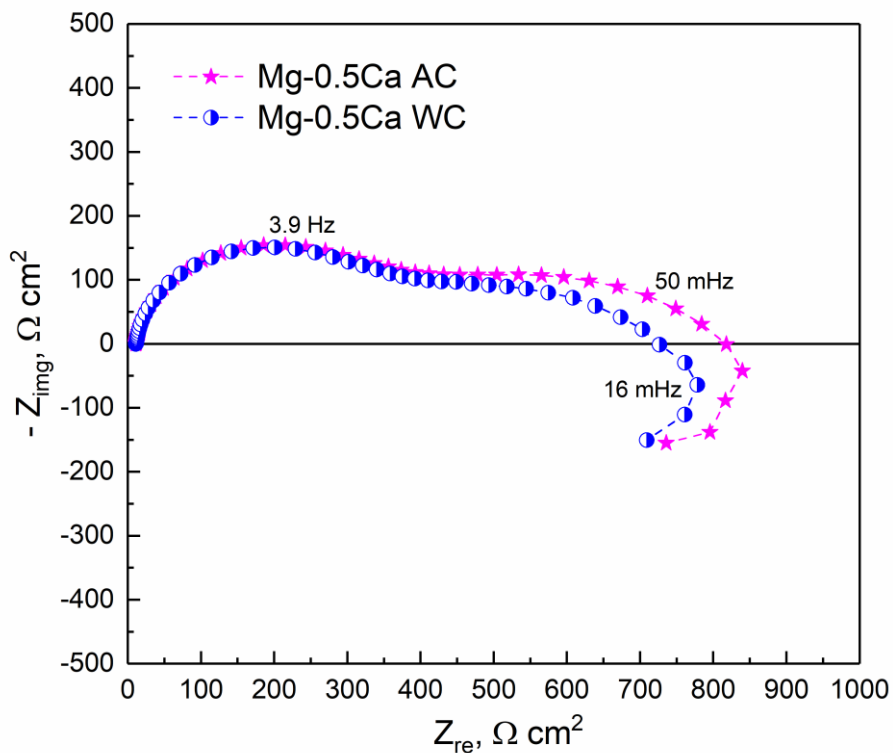

Fig. 10. Nyquist plots of the EIS spectra of Mg-0.5Ca anode after discharge at current density of 2 mA cm^{-2} for one hour in 3.5 wt.% NaCl solution.

5. Conclusions

In this work, Mg-0.5Ca alloys with various microstructures are prepared through different cooling routes. Afterwards, the effect of microstructure on the corrosion performance of Mg-0.5wt.%Ca binary alloys is studied through immersion tests combined with surface morphology analysis. Moreover, the discharge properties of primary Mg-air batteries using Mg-0.5Ca alloy anodes are measured to study the influence of the microstructure. The following conclusions are obtained from this work:

(1) The Mg-0.5Ca air-cooled alloy shows fine Mg_2Ca particles dispersing uniformly in Mg matrix and grain boundaries. After water-cooling, the grain size of Mg-0.5Ca alloy decreases slightly, and the second phases are distributed relatively continuously along the grain boundaries. In addition, more impurity-rich particles are found in the air-cooled alloy.

(2) Both Mg-0.5Ca alloys show remarkably low overall corrosion rates, enabling them to be attractive anode materials for aqueous Mg-air batteries with long-term storage. The corrosion rate of the water-cooled alloy is lower than that of the air-cooled material, because of the greater general corrosion behaviour. The localized corrosion of the air-cooled alloy is due to a large number of fine Mg_2Ca particles and more impurity-rich particles.

(3) During discharge, the water-cooled Mg-0.5Ca anode has a higher utilization efficiency and specific energy density than the air-cooled anode, attributed to the lower corrosion rate and low amount of detached undissolved grains. Discharge cracks in the air-cooled anode tend to become larger and then promote the emergence of the chunk effect. By contrast, discharge cracks in the water-cooled anode tend to penetrate along grain boundaries, leading to uniform discharge.

(4) Mg-air batteries fabricated with these two Mg-0.5Ca anodes show similar cell voltages as a result of the higher OCV of the air-cooled anode and higher discharge activity of the water-

cooled one. The water-cooled alloy could be a better anode material for Mg-air batteries under intermittent discharge due to the stable discharge voltage.

Data availability

The raw/processed data required to reproduce these findings cannot be shared at this time as the data also forms part of an ongoing study.

Reference

[1] F. Cheng, J. Chen, Metal-air batteries: from oxygen reduction electrochemistry to cathode catalysts, Chem Soc Rev, 41 (2012) 2172-2192. https://doi.org/10.1039/c1cs15228a.

[2] T. Zhang, Z. Tao, J. Chen, Magnesium–air batteries: from principle to application, Mater. Horiz., 1 (2014) 196-206. https://doi.org/10.1039/c3mh00059a.

[3] M.A. Rahman, X. Wang, C. Wen, High Energy Density Metal-Air Batteries: A Review, J. Electrochem. Soc. , 160 (2013) A1759-A1769. https://doi.org/10.1149/2.062310jes.

[4] R.P. Hamlen, E.C. Jerabek, J.C. Ruzzo, E.G. Siwek, Anodes for Refuelable Magnesium-Air Batteries, J. Electrochem. Soc. , 116 (1969) 1588-1592. https://doi.org/ 10.1149/1.2411622.

[5] Y.D. Milusheva, R.I. Boukoureshtlieva, S.M. Hristov, A.R. Kaisheva, Environmentally-clean Mg-air electrochemical power sources, Bulgarian Chemical Communications, 43 (2011) 42-47.

[6] C. Li, F. Cheng, W. Ji, Z. Tao, J. Chen, Magnesium microspheres and nanospheres: Morphology-controlled synthesis and application in Mg/MnO2 batteries, Nano Research, 2 (2009) 713-721. https://doi.org/10.1007/s12274-009-9075-y.

[7] M. Curioni, The behaviour of magnesium during free corrosion and potentiodynamic polarization investigated by real-time hydrogen measurement and optical imaging, Electrochim. Acta 120 (2014) 284-292. https://doi.org/10.1016/j.electacta.2013.12.109.

[8] D. Hoche, S.V. Lamaka, B. Vaghefinazari, T. Braun, R.P. Petrauskas, M. Fichtner, M.L. Zheludkevich, Performance boost for primary magnesium cells using iron complexing agents as electrolyte additives, Sci Rep, 8 (2018) 7578. https://doi.org/10.1038/s41598-018-25789-8.

[9] Y. Li, J. Ma, G. Wang, F. Ren, Y. Zhu, Investigation of Sodium Phosphate and Sodium Dodecylbenzenesulfunate as Electrolyte Additives for AZ91 Magnesium-Air Battery, J. Electrochem. Soc. , 165 (2018) A1713-A1717. https://doi.org/10.1149/2.0581809jes.

[10] M.A. Deyab, Decyl glucoside as a corrosion inhibitor for magnesium–air battery, J. Power Sources 325 (2016) 98-103. https://doi.org/10.1016/j.jpowsour.2016.06.006.

[11] M. Mayilvel Dinesh, K. Saminathan, M. Selvam, S.R. Srither, V. Rajendran, K.V.I.S. Kaler, Water soluble graphene as electrolyte additive in magnesium-air battery system, J. Power Sources 276 (2015) 32-38. https://doi.org/10.1016/j.jpowsour.2014.11.079.

[12] Y. Zhao, G. Huang, C. Zhang, C. Peng, F. pan, Effect of phosphate and vanadate as electrolyte additives on the performance of Mg-air batteries, Mater. Chem. Phys. , 218 (2018) 256-261. https://doi.org/10.1016/j.matchemphys.2018.07.037.

[13] S.V. Lamaka, B. Vaghefinazari, D. Mei, R.P. Petrauskas, D. Höche, M.L. Zheludkevich, Comprehensive screening of Mg corrosion inhibitors, Corrosion Science, 128 (2017) 224-240. https://doi.org/10.1016/j.corsci.2017.07.011.

[14] G. Huang, Y. Zhao, Y. Wang, H. Zhang, F. Pan, Performance of Mg–air battery based on AZ31 alloy sheet with twins, Materials Letters, 113 (2013) 46-49. https://doi.org/10.1016/j.matlet.2013.09.041.

[15] M. Yuasa, X. Huang, K. Suzuki, M. Mabuchi, y. Chino, Effects of Microstructure on Discharge Behavior of AZ91 Alloy as Anode for Mg-air Battery, Mater. Trans. , 55 (2014) 1202-1207. https://doi.org/10.2320/matertrans.MC201403.

[16] Y. Feng, W. Xiong, J. Zhang, R. Wang, N. Wang, Electrochemical discharge performance of the Mg–Al–Pb–Ce–Y alloy as the anode for Mg–air batteries, Journal of Materials Chemistry A, 4 (2016) 8658-8668. https://doi.org/10.1039/c6ta02574a.

[17] T. Zheng, Y. Hu, Y. Zhang, S. Yang, F. Pan, Composition optimization and electrochemical properties of Mg-Al-Sn-Mn alloy anode for Mg-air batteries, Materials & Design, 137 (2018) 245-255. https://doi.org/10.1016/j.matdes.2017.10.031.

[18] H. Xiong, K. Yu, X. Yin, Y. Dai, Y. Yan, H. Zhu, Effects of microstructure on the electrochemical discharge behavior of Mg-6wt%Al-1wt%Sn alloy as anode for Mg-air primary battery, J. Alloys Compd. , 708 (2017) 652-661. https://doi.org/10.1016/j.jallcom.2016.12.172.

[19] S. Yuan, H. Lu, Z. Sun, L. Fan, X. Zhu, WeiZhang, Electrochemical Performance of Mg-3Al Modified with Ga, In and Sn as Anodes for Mg-Air Battery, J. Electrochem. Soc. , 163 (2016) A1181-A11187. https://doi.org/10.1149/2.0371607jes.

[20] N. Wang, R. Wang, Y. Feng, W. Xiong, J. Zhang, M. Deng, Discharge and corrosion behaviour of Mg-Li-Al-Ce-Y-Zn alloy as the anode for Mg-air battery, Corrosion Science, 112 (2016) 13-24. https://doi.org/10.1016/j.corsci.2016.07.002.

[21] Y. Ma, N. Li, D. Li, M. Zhang, X. Huang, Performance of Mg–14Li–1Al–0.1Ce as anode for Mg-air battery, Journal of Power Sources, 196 (2011) 2346-2350. https://doi.org/10.1016/j.jpowsour.2010.07.097.

[22] X. Liu, S. Liu, J. Xue, Dishcarge performance of the magnesium anodes with different phase constitutions for Mg-air batteries, J. Power Sources 396 (2018) 667-674. https://doi.org/10.1016/j.jpowsour.2018.06.085.

[23] M. Deng, D. Hoeche, S. V. Lamaka, D. Snihirova, M. Zheludkevich, Mg-Ca binary alloys as anodes for primary Mg-air batteries, J. Power Sources 396 (2018) 109-118. https://doi.org/10.1016/j.jpowsour.2018.05.090.

[24] N. Wang, R. Wang, C. Peng, Y. Feng, Enhancement of the discharge performance of AP65 magnesium alloy anodes by hot extrusion, Corrosion Science, 81 (2014) 85-95. https://doi.org/10.1016/j.corsci.2013.12.005.

[25] N. Wang, R. Wang, C. Peng, Y. Feng, B. Chen, Effect of hot rolling and subsequent annealing on electrochemical discharge behavior of AP65 magnesium alloy as anode for seawater activated battery, Corrosion Science, 64 (2012) 17-27. https://doi.org/10.1016/j.corsci.2012.06.024.

[26] L. Wang, R. Wang, Y. Feng, M. Deng, N. Wang, Effect of Heat Treatment on Electrochemical Properties of Mg–9 wt.%Al–2.5 wt.%Pb Alloy in Sodium Chloride Solution, JOM 69 (2017) 2467-2470. https://doi.org/10.1007/s11837-017-2276-z.

[27] B. Campillo, C. Rodriguez, J. Genesca, O. Flores, L. Martinez, Effect of heat treatment on the efficiency of Mg anodes J. Mater. Eng. Perform. , 6 (1997) 449-453. https://doi.org/10.1007/s11665-997-0115-z

[28] M.H. Idris, H. Jafari, S.E. Harandi, M. Mirshahi, S. Koleyni, Characteristics of As-Cast and Forged Biodegradable Mg-Ca Binary Alloy Immersed in Kokubo Simulated Body Fluid,

Advanced Materials Research, 445 (2012) 301-306.

https://doi.org/10.4028/www.scientific.net/AMR.445.301.

[29] S. Koleini, M.H. Idris, H. Jafari, Influence of hot rolling parameters on microstructure and biodegradability of Mg–1Ca alloy in simulated body fluid, Materials & Design, 33 (2012) 20-25. https://doi.org/10.1016/j.matdes.2011.06.063.

[30] J.W. Seong, W.J. Kim, Development of biodegradable Mg-Ca alloy sheets with enhanced strength and corrosion properties through the refinement and uniform dispersion of the Mg(2)Ca phase by high-ratio differential speed rolling, Acta Biomater, 11 (2015) 531-542. https://doi.org/10.1016/j.actbio.2014.09.029.

[31] Y.S. Jeong, W.J. Kim, Enhancement of mechanical properties and corrosion resistance of Mg–Ca alloys through microstructural refinement by indirect extrusion, Corrosion Science, 82 (2014) 392-403. https://doi.org/10.1016/j.corsci.2014.01.041.

[32] D. Hoche, C. Blawert, S.V. Lamaka, N. Scharnagl, C. Mendis, M.L. Zheludkevich, The effect of iron re-deposition on the corrosion of impurity-containing magnesium, Phys Chem Chem Phys, 18 (2016) 1279-1291. https://doi.org/10.1039/c5cp05577f.

[33] G.L. Song, A. Atrens, Corrosion Mechanisms of Magnesium alloys, Adv. Eng. Mater. , 1 (1999) 11-33. https://doi.org/10.1002/(SICI)1527-2648(199909)1:1<11::AID-ADEM11>3.0.CO;2-N.

[34] G.L. Song, A. Atrens, D. StJohn, An Hydrogen Evolution Method for the Estimation of the Corrosion Rate of Magnesium Alloys, Magnesium Technology, (2001) 255-262.

https://doi.org/10.1002/9781118805497.ch44.

[35] Z. Shi, A. Atrens, An innovative specimen configuration for the study of Mg corrosion, Corros. Sci. , 53 (2011) 226-246. https://doi.org/10.1016/j.corsci.2010.09.016.

[36] M. Yuasa, X. Huang, K. Suzuki, M. Mabuchi, Y. Chino, Discharge properties of Mg–Al–Mn–Ca and Mg–Al–Mn alloys as anode materials for primary magnesium–air batteries,

Journal of Power Sources, 297 (2015) 449-456.

https://doi.org/10.1016/j.jpowsour.2015.08.042.

[37] L. Fan, H. Lu, The effect of grain size on aluminum anodes for Al–air batteries in alkaline electrolytes, Journal of Power Sources, 284 (2015) 409-415.

https://doi.org/10.1016/j.jpowsour.2015.03.063.

[38] M.C. Lin, C.Y. Tsai, J.Y. Uan, Electrochemical behaviour and corrosion performance of Mg–Li–Al–Zn anodes with high Al composition, Corrosion Science, 51 (2009) 2463-2472.

https://doi.org/10.1016/j.corsci.2009.06.036.

[39] Y.Y. Chen, T. Duval, U.D. Hung, J.W. Yeh, H.C. Shih, Microstructure and electrochemical properties of high entropy alloys—a comparison with type-304 stainless steel, Corrosion Science, 47 (2005) 2257-2279. https://doi.org/10.1016/j.corsci.2004.11.008.

[40] Z. Li, X. Gu, S. Lou, Y. Zheng, The development of binary Mg-Ca alloys for use as biodegradable materials within bone, Biomaterials, 29 (2008) 1329-1344.

https://doi.org/10.1016/j.biomaterials.2007.12.021.

[41] M. Mohedano, B.J.C. Luthringer, B. Mingo, F. Feyerabend, R. Arrabal, P.J. Sanchez-Egido, C. Blawert, R. Willumeit-Römer, M.L. Zheludkevich, E. Matykina, Bioactive plasma electrolytic oxidation coatings on Mg-Ca alloy to control degradation behaviour, Surface and Coatings Technology, 315 (2017) 454-467. https://doi.org/10.1016/j.surfcoat.2017.02.050.

[42] R.-C. Zeng, W.-C. Qi, H.-Z. Cui, F. Zhang, S.-Q. Li, E.-H. Han, In vitro corrosion of as-extruded Mg–Ca alloys—The influence of Ca concentration, Corrosion Science, 96 (2015) 23-31. https://doi.org/10.1016/j.corsci.2015.03.018.

[43] Z. Qiao, Z. Shi, N. Hort, N.I. Zainal Abidin, A. Atrens, Corrosion behaviour of a nominally high purity Mg ingot produced by permanent mould direct chill casting, Corrosion Science, 61 (2012) 185-207. https://doi.org/10.1016/j.corsci.2012.04.030.

[44] N.T. Kirkland, N. Birbilis, M.P. Staiger, Assessing the corrosion of biodegradable magnesium implants: a critical review of current methodologies and their limitations, Acta Biomater, 8 (2012) 925-936. https://doi.org/10.1016/j.actbio.2011.11.014.

[45] A. Atrens, G.-L. Song, F. Cao, Z. Shi, P.K. Bowen, Advances in Mg corrosion and research suggestions, Journal of Magnesium and Alloys, 1 (2013) 177-200. https://doi.org/10.1016/j.jma.2013.09.003.

[46] F. Cao, Z. Shi, G.-L. Song, M. Liu, A. Atrens, Corrosion behaviour in salt spray and in 3.5% NaCl solution saturated with Mg(OH)2 of as-cast and solution heat-treated binary Mg–X alloys: X=Mn, Sn, Ca, Zn, Al, Zr, Si, Sr, Corros. Sci. , 76 (2013) 60-97. https://doi.org/10.1016/j.corsci.2013.06.030.

[47] Y.L. Liu, S.B. Kang, Solidification and segregation of AI-Mg alloys and influence of alloy composition and cooling rate, Mater. Sci. Technol. , 13 (1997) 331-336. https://doi.org/10.1179/mst.1997.13.4.331.

[48] G.Y. Yuan, Z.L. Liu, Q.D. Wang, W.J. Ding, Microstructure refinement of Mg–Al–Zn–Si alloys, Mater. Lett. , 56 (2002) 53-58. https://doi.org/10.1016/S0167-577X(02)00417-2.

[49] A. Singh, Y. Osawa, H. Somekawa, T. Mukai, Effect of Solidification Cooling Rate on Microstructure and Mechanical Properties of an Extruded Mg-Zn-Y Alloy, Metals, 8 (2018) 337. https://doi.org/10.3390/met8050337.

[50] G. Song, A. Atrens, M. Dargusch, Influence of microstructure on the corrosion of diecast AZ91D, Corros. Sci. , 41 (1998) 249-273. https://doi.org/10.1016/S0010-938X(98)00121-8.

[51] A.D. Südholz, N.T. Kirkland, R.G. Bucheheit, N. Birbilis, Electrochemical Properties of Intermetallic Phases and common impurity elements in Mg alloys, Electrochem. Solid-State Lett. , 14 (2011) C5-C7. https://doi.org/10.1149/1.3523229.

[52] N.T. Kirkland, N. Birbilis, J. Walker, T. Woodfield, G.J. Dias, M.P. Staiger, In-vitro dissolution of magnesium-calcium binary alloys: clarifying the unique role of calcium

additions in bioresorbable magnesium implant alloys, J Biomed Mater Res B Appl Biomater, 95 (2010) 91-100. https://doi.org/10.1002/jbm.b.31687.

[53] M. Mandal, A.P. Moon, G. Deo, C.L. Mendis, K. Mondal, Corrosion behavior of Mg–2.4Zn alloy micro-alloyed with Ag and Ca, Corros. Sci. , 78 (2014) 172-182. https://doi.org/10.1016/j.corsci.2013.09.012.

[54] J.W. Seong, W.J. Kim, Mg-Ca binary alloy sheets with Ca contents of ≤1 wt.% with high corrosion resistance and high toughness, Corros. Sci. , 98 (2015) 372-381. https://doi.org/10.1016/j.corsci.2015.05.068.

[55] M. Andrei, D.d. Gabriele, P.L. Bonora, D. Scantlebury, Corrosion behaviour of magnesium sacrificial in tap water, Mater. Corros. , 54 (2003) 5-11. https://doi.org/10.1002/maco.200390010.

[56] G.A. Marsh, E. Schaschl, The Difference Effect and the Chunk Effect, J. Electrochem. Soc. , 107 (1960) 960-965. https://doi.org/10.1149/1.2427579

[57] G. Song, A. Atrens, D. Stjohn, J. Nairn, Y. Li, The electrochemical corrosion of pure magnesium in 1 N NaCl, Corros. Sci. , 39 (1997) 855-875. https://doi.org/10.1016/S0010-938X(96)00172-2.

[58] R. Glicksman, The Performance of Zinc, Magnesium and Aluminum Primary Cell Anodes. A review, J. Electrochem. Soc. , 106 (1959) 457-464. https://doi.org/10.1149/1.2427380

[59] N. Birbilis, K.D. Ralston, S. Virtanen, H.L. Fraser, C.H.J. Davies, Grain character influences on corrosion of ECPAed pure magnesium, Corrosion Enginnering, Science and Technology, 45 (2010) 224-230. https://doi.org/10.1179/147842209X12559428167805.

[60] D. Song, A. Ma, J. Jiang, P. Lin, D. Yang, J. Fan, Corrosion behavior of equal-channel-angular-pressed pure magnesium in NaCl aqueous solution, Corros. Sci. , 52 (2010) 481-490. https://doi.org/10.1016/j.corsci.2009.10.004.

[61] N. Munichandraiah, Electrochemical impedance studies of a decade-aged magnesium/manganese dioxide primary cell, J. Appl. Electrochem. , 29 (1999) 463-471.

[62] N. Sato, Anodic Breakdown of Passive Films on Metals, J. Electrochem. Soc. , 129 (1982) 255-260. https://doi.org/10.1149/1.2123808